Journal of Materials Chemistry A

ROYAL SOCIETY OF CHEMISTRY

PAPER

View Article Online
View Journal | View Issue

Cite this: J. Mater. Chem. A, 2022, 10, 22042

Suppressing H_2O_2 formation in the oxygen reduction reaction using Co-doped copper oxide electrodes†

Sekhar Kumar Biswal and Chinmoy Ranjan *

Received 31st May 2022
Accepted 18th September 2022

DOI: 10.1039/d2ta04349a

rsc.li/materials-a

Transition metal oxides form the basis of promising oxygen reduction electrocatalysts due to their low cost, high activity, and abundance on the planet. A new class of Co-doped CuO_x (Cu[Co]O_x/Au) catalyst was found to exhibit high activity and selectivity for the complete reduction of oxygen to water. Cu-rich doped-$Cu_{0.8}Co_{0.2}O_x$/Au electrodes exhibited nearly 97.5% selectivity for water compared to either CuO_x/Au (80%) or CoO_x/Au (70%). $Cu_{0.8}Co_{0.2}O_x$/Au exhibited higher activity, stability, and better selectivity over a wide potential range when compared to well-known ORR catalysts such as Pt. *In situ* Raman spectroscopy revealed that the introduction of Co into CuO_x resulted in the formation of under-coordinated Co centers within CuO_x frameworks. These under-coordinated Co centers act as active sites for the scission of O–O bonds resulting in preferential formation of 4e reduction products. The doped electrode also demonstrated a superior hydrogen peroxide reduction ability.

Introduction

The oxygen reduction reaction (ORR) is at the heart of electrochemical reactions such as fuel cells, metal–air batteries, and industrial processes such as the chloralkali process.[1–3] Even with decades of research, the best ORR catalysts still show high overpotentials and insufficient selectivity for the total reduction of oxygen to water.[1,4] The formation of hydrogen peroxide as a side product results in energy loss and corrosion of electrodes. Platinum has been the most well-known catalyst for the ORR. Besides being scarce, Pt also remains susceptible to degradation.[5] As a result, the search for active, selective, and cost-effective catalysts continues.

Transition metal oxide (TMO) based catalysts are abundant and show promise to meet these requirements, especially in alkaline media.[6,7] TMOs act as good catalysts because of the availability of a large number of oxidation states and tunable redox properties based on altering the immediate coordination environment around the central metal atom. Besides this, TMOs show good structural stability and often sufficient electronic conductivity to act as good electrodes in the alkaline medium. Besides TMOs, composite catalysts such as metals on nitrogen-doped carbon (*e.g.* Fe-N-C) have also gained attention in recent times as active materials that can substitute the use of Pt.[8–10]

The overall reactivity of catalyst depends on a host of factors that include the binding energy of intermediate adsorbates, the nature of the solvent and how well the catalyst solution interface handles reactants and products (*e.g.* stiffness of the electrochemical double layer).[11] Reactivity models based on the binding energy of adsorbates (specially obtained from DFT calculations) have significantly influenced catalyst development in the last two decades.[12,13] In the context of the ORR using perovskite catalysts, Suntivich *et al.* have correlated OH binding energy at metal sites with the electron occupancy of the e_g orbitals.[14,15] Li *et al.* have argued that O binding to TMO sites remains weak, which in turn makes O–O bond cleavage kinetically difficult.[16] This relationship although insightful is of limited value when defect sites, multiply coordinated oxygen ions or lattice oxygen get involved.[16] Cao *et al.* have discussed lattice oxygen involvement and surface exchange in the context of O_2 reduction in solid oxide electrodes.[17] Creating synthetic methods to introduce interface effects, creating unusual oxygen binding sites and introducing defect sites can be a good strategy to overcome reactivity limitations on pristine surfaces. A lot depends on how the catalysts are actually synthesized. Temperature at which catalysts are created results in a certain degree of defects, which can be considered as active sites for the OER.[18]

Doped transition metal oxide compounds that incorporate two or more metallic elements into one oxide framework have been the focus of extensive research in oxygen electrocatalysis.[19] The mixing of oxides can result in many effects. In certain cases, the crystal structures of the fundamental oxides are altered.

Department of Inorganic and Physical Chemistry, Indian Institute of Science, Bangalore-560012, India. E-mail: ranjan@iisc.ac.in

† Electronic supplementary information (ESI) available: Additional data from various experiments. The SEM and EDX spectra of electrodes, ICP-OES measurements, additional electrochemical data pertaining to the calculation of the ECSA, electron transfer numbers, and yield of H_2O_2, and estimation of kinetic currents. See https://doi.org/10.1039/d2ta04349a

Catalytic effects can result from the alteration of the crystal structure of active components. Ad-atoms can enter the crystal structure of the active component and alter it electronically resulting in redox property modulation. Besides these additives can alter the electron conduction framework by altering the conductivity of the electrodes.[15,20] The coordination environment of metals can be different depending on the inherent preference of metal sites for a certain coordination of oxygen. The doping of different size ions into fundamental perovskite structures has been used to enhance oxide ion conductivity and alter electronic conductivity in solid oxide electrodes.[21,22]. TMOs such as cobalt and copper-based oxides have recently received a lot of attention due to their bifunctionality (OER and ORR), low cost, and high catalytic activity.[23–25]

Metal ions can naturally prefer different types of oxygen coordination environments. For example, some metal ions might prefer an octahedral oxygen coordination whereas other metal ions might prefer a square planar coordination of oxygen ions. Mixing two such metal ions, with dissimilar preference for oxygen coordination environments, within one composite framework can result in significant stress within the structure. Such materials can result in sites with stress or unsaturation akin to edge sites on metal surfaces such as Pt or Au or defect sites within oxides. Coordinative unsaturation is a known requirement in transition metal-based catalysts of molecular origin.[26]

Stewart *et al.* have reported enhanced peroxide degradation on a Cu/CuO(OH)$_x$ type electrode.[27] Yan *et al.* have demonstrated the activity of Cu_2O nanoparticles supported on reduced graphene oxide (rGO) for the ORR. Furthermore, they have argued for the use of a conducting substrate such as rGO due to lack of sufficient electronic conductivity in Cu_2O.[28] Cu–Co mixed oxides have also been tested for application in the OER and ORR. Vincent *et al.* carried out catalyst loading optimization studies of ORR activity for Cu incorporated cobalt oxide catalysts on GC electrodes.[29] Grewe *et al.* investigated ordered mesoporous composite materials (Co_3O_4–$CuCo_2O_4$).[30] De Koninck *et al.* demonstrated improved electron transfer numbers for Vulcan when $CuCo_2O_4$ was added to the composite.[31] Niu *et al.* investigated the OER activity of a CuO_x nanoarray film (NF) doped with transition metals such as Fe, Co, and Ni.[32] They discovered that, in comparison to Fe and Ni, the addition of Co showed considerably enhanced electrochemical oxygen evolution activity. They have attributed the increase in the OER activity to several effects that include the alternation of the cobalt active site, the transformation of Cu_2O to CuO, and the modification of the material morphology.[32] Chen *et al.* found that incorporating Ce into CuO_x increases OER activity, with the highest OER activity reported when 6.9% Ce is incorporated into the CuO_x framework. The authors reported that the most active Ce modified CuO_x catalyst (6.9% Ce) resulted in ~3.3 times the activity of pure CuO_x. They ascribe the increased activity to an increase in the Ce^{4+} concentration and a change in the catalyst structure.[33]

It is challenging to assign specific roles to metal centers within mixed oxide compositions and generic trends remain difficult to establish even with detailed control on both synthesis and diagnostics. In a dynamic catalytic environment, several factors such as potential, reactants, electrolytes, and even operational history (*e.g.*, activation protocols) can significantly influence the activity of the material. Besides this, the electrode must maintain significant electronic conductivity to and from the active sites during electrocatalysis. New investigative methodologies continue to evolve. *In situ*/*operando* spectroscopic methods can now provide insights into the catalytic environment during operation, helping in a better understanding of catalysis in action. Deng *et al.* have carried out *in situ* Raman spectroscopy studies on Cu(OH)$_x$ films for oxygen evolution.[34] Besides this, helpful theoretical models have evolved that have directed catalyst search and development.[14,15]

In the ORR, the oxygen molecule can be electrochemically reduced to water *via* either a direct four-electron (4e) reduction pathway or to hydrogen peroxide *via* a two-electron (2e) reduction pathway.[5,35] The 4e pathway resulting in H_2O is preferred in fuel cells, and any H_2O_2 formed from a 2e pathway is undesirable as it is corrosive and can diffuse across the device degrading the catalyst, support, and the gas diffusion layer, eventually destroying the electrode.[36,37]

In this study, we prepared a series of doped catalysts from copper and cobalt oxide *i.e.*, Cu[Co]O$_x$ with varying Co/Cu ratios supported on Au using a combination of electroless deposition and thermal treatment. The synthesis method allowed for systematic variation of the Cu and Co composition. The catalyst activity for the ORR and its selectivity for the 4e process were evaluated using rotating ring disc electrode voltammetry. Cu-rich compositions showed excellent activity and very high selectivity for 4e pathways across a wide range of potentials relevant for fuel cells. A comparison with the benchmark Pt catalyst showed higher activity, improved selectivity, and better stability for Cu[Co]O$_x$/Au. *In situ* spectroscopy has made it simpler to track this structural evolution of catalyst materials based on a variety of conditions that include composition, nature of the electrolyte, and applied potential. In this paper, *in situ* Raman spectroscopy was used to track the evolution of the catalyst structure during the ORR. Supporting studies were carried out using XPS and electron microscopy. We have shown that the presence of Co modulates not only the redox behavior of Cu but also influences the phase in which these Cu redox centers appear. The incorporation of Co into the CuO_x bonding framework results in under-coordinated Co species, which form active sites for the ORR. We have argued that such under-coordinated Co species can enhance the binding of intermediates such as OOH* and O* resulting in improved ORR activity and higher selectivity for the 4e pathway.

Experimental section

For synthesis, cobalt(II) sulfate heptahydrate ($CoSO_4 \cdot 7H_2O$, ≥99%) was obtained from Sigma Aldrich. Copper(II) nitrate trihydrate ($Cu(NO_3)_2 \cdot 3H_2O$, 99.0%) was obtained from Thomas Baker (Chemicals) Pvt Limited. Sodium hydroxide (NaOH, SUPRAPUR) was obtained from Merck. High purity (99.99%) O_2 was used in all experiments. All electrolytes were prepared with deionized water with a specific resistance of 18 MΩ. All chemicals were used as received.

Catalysts were prepared using an electroless deposition method followed by thermal annealing at 300 °C for 3 hours in air. Precursor solutions were prepared by mixing stoichiometric amounts of Cu $(NO_3)_2 \cdot 3H_2O$ and $CoSO_4 \cdot 7H_2O$ (*viz.* 2 : 8, 4 : 6, 6 : 4, 8 : 2, 9 : 1, and 9.5 : 0.5 ratios of Cu : Co) in 10 ml of deionized water. The total concentration of metal ions was maintained at 0.065 M. The mixed solutions were then transferred into a container. The electrode was prepared by immersing an electrochemically cleaned Au disc (polycrystalline, 5 mm diameter) into the solutions for 5 minutes followed by thermal treatment. Catalysts have been indicated by their formal compositions, *e.g.*, $Cu_{0.8}Co_{0.2}O_x$/Au implies that the catalyst was prepared by immersing the Au substrate in a solution containing the precursor ions in a ratio of 8 : 2. The actual compositions were found to be close to the formal compositions as verified by EDX and ICP-OES (Fig. S1–S4 and Table S1†).

A polycrystalline Au foil was used as a catalyst substrate for the *in situ* electrochemical Raman spectroscopy experiment. The Au foil was roughened electrochemically by using a method developed by Liu *et al.*[38] The method involves oxidation–reduction potential scanning cycles (for 25 cycles) between −0.28 V (hold time 10 s) and 1.22 V (hold time 5 s) *vs.* Ag/AgCl in 0.1 M NaCl solution at a scan rate of 500 mV s^{-1}[38] The roughened Au was rinsed in ultrapure water and further electrochemically cleaned by cycling.[39]

Electrochemical measurements

All the electrochemical experiments were carried out in a three electrode cell using a VMP3 potentiostat from BioLogic Science Instruments. A platinum wire and an Ag/AgCl/KCl (sat) electrode were used as counter and reference electrodes, respectively. All the measurements were performed in 0.1 M NaOH. All the reported potentials have been converted to the reversible hydrogen electrode (RHE) reference using $E_{RHE} = E_{Ag/AgCl} + 0.0591pH + E^{\circ}_{Ag/AgCl}$, unless explicitly mentioned. The cyclic voltammetry (CV) experiments were conducted at a scan rate of 20 mV s^{-1}, and the reported linear sweep voltammetry (LSV) curves were recorded at a scan rate of 5 mV s^{-1}. For the ORR, the electrolyte was saturated with O_2 by vigorous bubbling for 30 minutes, and a blanket of O_2 cover was maintained throughout the measurements. Rotating ring disc electrode (RRDE) experiments were carried out to measure the activity and peroxide selectivity of various electrodes using a RRDE setup from Pine Instruments. The disc electrode was under a variable potential control as per the experiment. The ring (Pt) electrode was maintained at 1.5 V to oxidize the H_2O_2 (under diffusion control) generated at the disc. The reported ring currents have been corrected as per a measured collection efficiency of 25%.

Structural characterisation

Scanning electron microscopy (SEM) and Energy Dispersive X-ray analysis (EDX) (JEOL SEM IT 300) were used to examine the surface morphologies and elemental ratios of samples.

High-resolution transmission electron microscopy (HRTEM) images were obtained using a FEI Titan Themis 300. Samples were prepared by dispersing the sample in hexane (HPLC grade) and then drop-casting onto a lacey carbon nickel TEM grid. Conventional bright-field (BF) TEM and HRTEM images of the samples were collected at an accelerating voltage of 300 keV. High Angle Annular Dark Field (HAADF) imaging was carried out in STEM mode. Thin-film X-ray diffraction (XRD) patterns (Grazing Incidence of Diffraction (GID) mode) were collected using a Bruker D8 discover X-ray diffractometer with Cu K_α radiation.

X-ray photoelectron spectroscopy (XPS) and Auger electron spectroscopy (AES) of catalytic samples were carried out using a Thermo Scientific K-Alpha XPS setup with an Al K_α source. A focus spot size of 400 micrometers was used. A pass energy value of 50.0 eV and a scan step size of 0.10 eV were used. The reference C 1s signal at 284.8 eV was used to correct all the reported binding energies.

Inductively Coupled Plasma Optical Emission Spectroscopy (ICP-OES) (PerkinElmer Avio 200 ICP Optical Emission Spectroscopy) was used for the elemental analysis of metal ions in various electrodes. More details of ICP-OES measurements are provided in the ESI.†

The Raman spectra were collected using a Renishaw In-Via Raman microscope with an excitation wavelength of 785 nm. The *in situ* electrochemical Raman spectra were obtained in O_2 saturated 0.1 M NaOH solution using a custom-made three-electrode Teflon cell with a platinum wire as the counter electrode and Ag/AgCl (Innovative Instruments, USA) as the reference electrode. *In situ* Raman measurements were collected using a previously published setup.[40] For submerged *in situ* samples, Raman spectra were collected for an exposure time of 15 s (averaged over two accumulations) with a source laser power of 30 mW. During *in situ* experiments, the potential was stepped to the desired value and held for six minutes. Raman collection was started after 1 minute of application of each potential step. The Raman spectrometer was calibrated using a 520.5 cm^{-1} peak of Si for all experiments.

Results and discussion

Structure and composition characterisation

Doped-Cu[Co]O_x/Au electrodes with various combinations of Cu and Co were prepared on Au foil and electrochemically tested for the ORR. The actual deposited composition on the Au foil was found to be close to the composition of the deposition bath using both ICP-OES and SEM-EDX measurements (Fig. S1–S4 and Table S1†).

Fig. 1(a) shows an optical image of the as-prepared $Cu_{0.8}$-$Co_{0.2}O_x$/Au catalyst. TEM-based analysis was performed on the Cu[Co]O_x compound by scratching off the deposited oxide from the Au-substrate onto a Ni–Carbon TEM grid. Particles in the range of 5–20 nm can be seen (Fig. 1(b)). Elemental mapping was carried out using EDX in the high-angle annular dark-field scanning transmission electron microscopy (HAADF-STEM) mode (Fig. 1(c)). It showed that Cu and Co were distributed homogeneously across the sample. The schematic model shown

in Fig. 1(d) illustrates the general heterogeneous morphology of the deposited Cu[Co]O_x catalyst (green) on an Au substrate (yellow). The catalyst covers various parts of the substrate, but sections of Au remain exposed to the electrolyte. This is further confirmed by Raman Spectroscopy, where only the green regions in Fig. 1(a) and (d), show an oxide signal. X-ray diffraction patterns were collected using grazing incidence diffraction geometry to maximize the signal from the deposited oxide. The XRD pattern (Fig. 1(e)) of the as-prepared oxide material shows the clear presence of the CuO phase, besides strong peaks originating from the Au substrate. No peaks from known CoO_x phases were observed. It is likely that CoO_x exists in small X-ray amorphous domains. SEM-EDX elemental analysis was employed to identify the relative composition of Cu and Co in the as-prepared Cu[Co]O_x/Au samples (Fig. 1(f)). The measured Cu/Co ratios from SEM-EDX match adequately with the concentrations of Cu and Co ions present in the precursor solutions.

Electrochemical characterization

ORR polarisation curves for Cu[Co]O_x/Au catalysts obtained using an RRDE setup are shown in Fig. 2(a). Selectivity for hydrogen peroxide formation was measured by holding the ring electrode at 1.5 V, where the oxidation of the HO_2^- ion ($HO_2^- + OH^- \rightarrow O_2 + H_2O + 2e^-$) is diffusion-limited.[5] Further details of the calculation of H_2O_2 selectivity are provided in the ESI (ESI note 1†). The Cu[Co]O_x/Au electrodes were found to perform much better than the pure electrodes in general. Specifically, the electrodes rich in the Cu content (Cu_yCo_{1-y}, $y \geq 0.6$) showed high ORR activity. The pure-CuO_x/Au and CoO_x/Au catalysts produce large amounts of peroxide (~20–30%), whereas the Cu[Co]O_x/Au electrodes yielded significantly less peroxide (less than 10%). Specifically, the Cu-rich electrodes ($Cu_{0.8}Co_{0.2}O_x$/Au and $Cu_{0.6}Co_{0.4}O_x$/Au) were found to produce minimal amounts of peroxide across a large potential window relevant for the ORR in fuel cells (0.9–0.6 V). The ORR activity and peroxide selectivity for various electrodes at 0.6 V are reported in Fig. 2(b). The ORR activity was found to increase with an increase in the Cu content. The composition with $y = 0.9$ showed the highest ORR activity. A further increase in the Cu content ($y = 0.95$) resulted in a slight decrease in ORR activity. The peroxide selectivity was found to be lowest for $y = 0.8$ with a slight increase in peroxide formation observed with richer compositions ($y > 0.8$). The composition of $y = 0.8$ was found to provide an optimum mix of high ORR activity and low peroxide selectivity and a good representative of Cu[Co]O_x/Au type electrodes. This composition was chosen for further characterization.

The electrodes were further evaluated using cyclic voltammetry (Fig. 2(c), (d), and S5†) between 1.1 and 0 V. In pure CoO_x/Au, significant redox features appear only upon oxygen reduction (Fig. 2(d)). The similarity in the cyclic voltammograms of $Cu_{0.8}Co_{0.2}O_x$/Au and pure CuO_x/Au electrodes indicate that Cu remains redox-active (Fig. 2(c)). The peaks of the CV and associated Cu redox features are tabulated in Table 1.

The oxidation and reduction peaks observed in the CV (Fig. 2(c)) are labeled O^n and R^n respectively. Significant similarities of redox features can be identified in the CuO_x/Au electrode compared to Cu CVs available in the literature.[41,43] Table 1 lists O^n and R^n peaks along with assignments from the

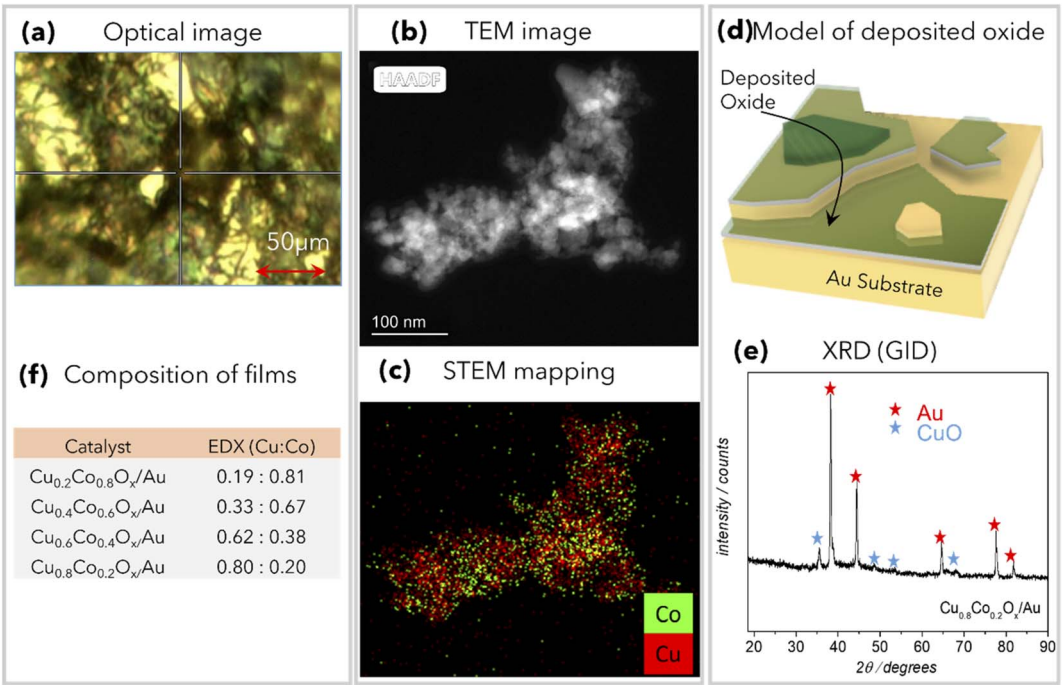

Fig. 1 Catalyst characterization: (a) optical image, (b) TEM image, and (c) STEM mapping showing Co and Cu distribution in the catalyst, (d) model of the Co-doped CuO_x electrode material showing an oxide layer on an Au substrate, (e) XRD pattern of $Cu_{0.8}Co_{0.2}O_x$/Au, and (f) metal composition of the as-prepared oxides determined by SEM-EDX.

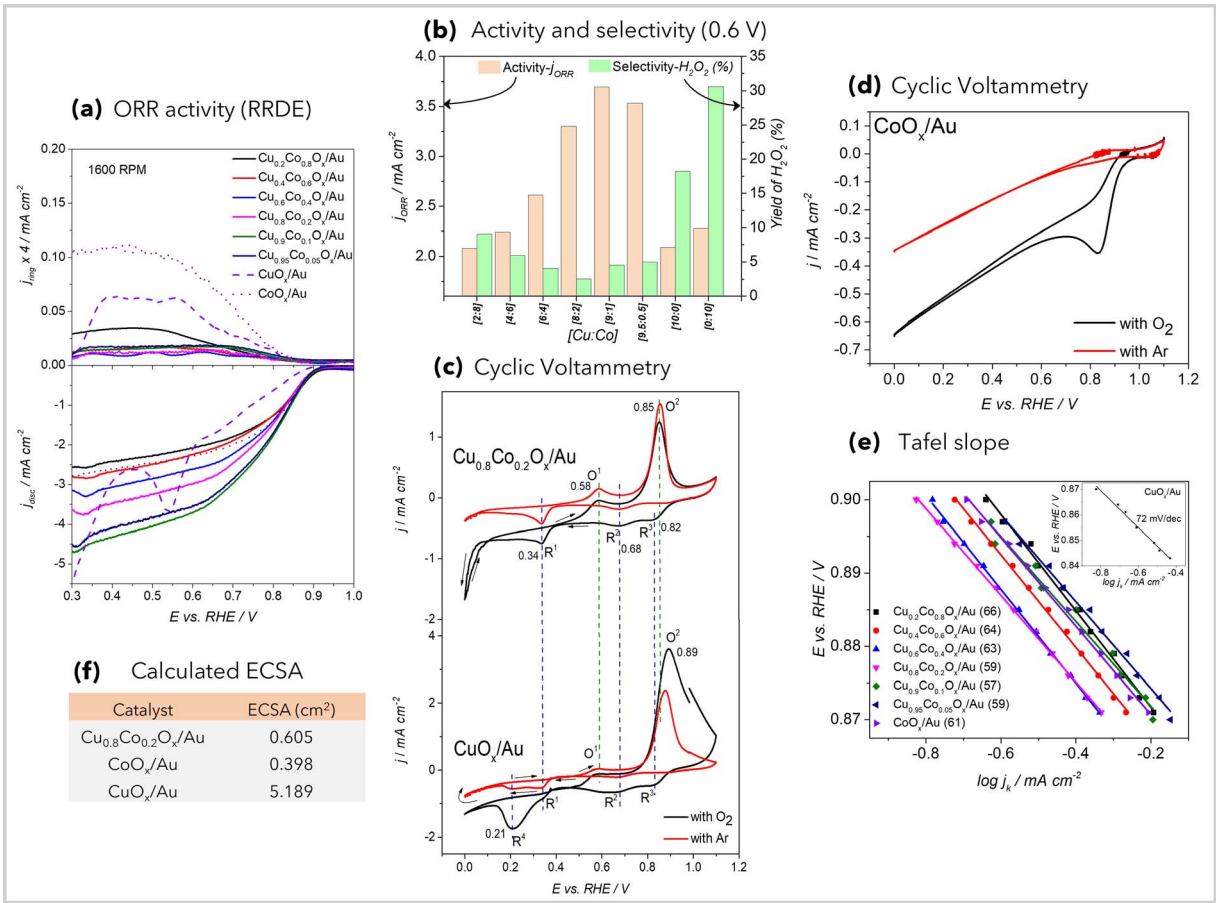

Catalyst	ECSA (cm^2)
$Cu_{0.8}Co_{0.2}O_x$/Au	0.605
CoO_x/Au	0.398
CuO_x/Au	5.189

Fig. 2 Electrochemical measurements: (a) results from RRDE experiments obtained from doped-Cu[Co]O_x/Au and pure-CoO_x/Au and CuO_x/Au electrodes in O_2 saturated 0.1 M NaOH. The disc electrodes were prepared by the deposition of oxides on an Au disc of 5 mm diameter. The ring disc setup was rotated at 1600 rpm. A potential scan rate of 5 mV s^{-1} was used for measuring ORR activity at the disc electrode. The Pt ring electrode was held at 1.5 V for the collection of H_2O_2 generated at the disc, (b) activity and selectivity of various doped-Cu[Co]O_x/Au, pure-CoO_x/Au and CuO_x/Au are shown at 0.6 V, (c) cyclic voltammograms of $Cu_{0.8}Co_{0.2}O_x$/Au and CuO_x/Au are shown in both argon and oxygen saturated solutions. The oxidation peaks and reduction peaks are labeled O^n and R^n respectively, (d) cyclic voltammogram of the CoO_x/Au electrode. A potential scan rate of 20 mV s^{-1} was used for cyclic voltammetry and (e) Tafel plots for various Cu[Co]O_x/Au compounds and pure-CoO_x/Au and CuO_x/Au (in the inset) electrodes. The Tafel slope values are indicated near the legend within brackets. The kinetic current used in Tafel plots was extracted from RDE experiments using the Koutecky–Levich methodology and (f) electrochemically active surface area of $Cu_{0.8}Co_{0.2}O_x$/Au, CuO_x/Au and CoO_x/Au was calculated by measuring the double-layer capacitance of the electrodes.

literature. O^1 is associated with the formation of thin layer Cu^{1+} oxide from Cu^0, whereas O^2 is associated with the transformation of $Cu^{0,1+}$ into Cu^{2+}. The differences between doped-Cu[Co]O_x/Au and pure Cu electrodes are reflected in the small changes in the positions of the peaks.[41] In an Ar environment, in the anodic sweep, the position of O^1 is unaffected, and the O^2 peak occurs at a lower potential in the context of the Cu[Co]O_x/Au sample compared to CuO_x/Au. The reduction features

Table 1 Redox peaks of Cu[Co]O_x/Au and CuO_x/Au have been tabulated. The oxidation and reduction peaks are labeled in Fig. 2(c). Reference potentials are taken from Caballero-Briones, F *et al.*[41,42]

	Peak position (E/V *vs.* RHE)			
Peak name	$Cu_{0.8}Co_{0.2}O_x$/Au	CuO_x/Au	Peak assigned	Reference potential (E/V *vs.* RHE)
O^1	0.58	0.58	$Cu^0 \rightarrow Cu^{1+}$	~0.59
O^2	0.85	>0.85	Cu^0, $Cu^{1+} \rightarrow Cu^{2+}$	~0.85 and 1.02
R^1	0.34	0.34	Cu^{2+}, $Cu^{1+} \rightarrow Cu^0$	—
R^2	0.68	0.68	$Cu^{2+} \rightarrow Cu^{1+}$	~0.47
R^3	0.82	0.82	ORR	—
R^4	—	0.21	Cu^{2+}, $Cu^{1+} \rightarrow Cu^0$	~0.15

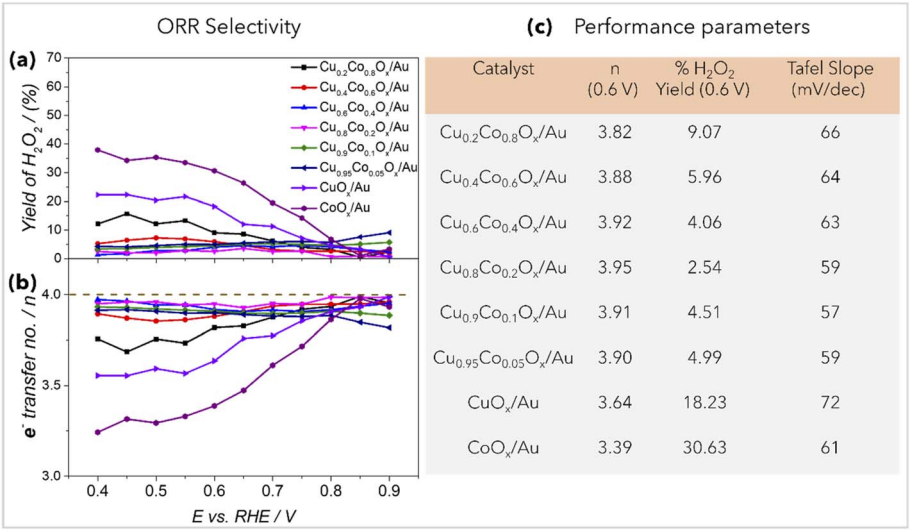

(c) Performance parameters

Catalyst	n (0.6 V)	% H_2O_2 Yield (0.6 V)	Tafel Slope (mV/dec)
$Cu_{0.2}Co_{0.8}O_x$/Au	3.82	9.07	66
$Cu_{0.4}Co_{0.6}O_x$/Au	3.88	5.96	64
$Cu_{0.6}Co_{0.4}O_x$/Au	3.92	4.06	63
$Cu_{0.8}Co_{0.2}O_x$/Au	3.95	2.54	59
$Cu_{0.9}Co_{0.1}O_x$/Au	3.91	4.51	57
$Cu_{0.95}Co_{0.05}O_x$/Au	3.90	4.99	59
CuO_x/Au	3.64	18.23	72
CoO_x/Au	3.39	30.63	61

Fig. 3 (a) H_2O_2 yields and (b) electron transfer numbers are shown as a function of potential for various electrodes. (c) Performance parameters; electron transfer numbers (n), % H_2O_2 yield, and Tafel slopes are listed for various evaluated catalysts.

associated with Cu in the literature essentially show two dominant peaks. The one corresponding to Cu^{2+} to Cu^{1+} reduction occurs at a higher potential (~0.47 V) and is mostly insensitive to OH^- ion concentration.[42] The second peak associated with Cu^{2+} to Cu^0 and Cu^{1+} to Cu^0 reduction (small amount) occurs at around 0.15 V and is known to respond to OH^- ion concentration.[42] These features are associated with peaks R^1 (at 0.34 V) and R^4 (at 0.15 V) in the CuO_x/Au electrode. The reduction peak R^4 is suppressed in the Cu[Co]O_x/Au. In the presence of O_2, whereas R^4 is prominent in pure CuO_x/Au, it's practically absent in the doped-Cu[Co]O_x/Au electrode. In the presence of O_2, a strong reduction feature appears at 0.1 V in the Cu[Co]O_x/Au electrode which is absent in pure CuO_x/Au. The presence of O_2 in solution results in the peak R^3, associated with the ORR, on either electrode. In general, the prominent redox features of CuO_x electrodes are observable with both Cu[Co]O_x/Au and CuO_x/Au, but the peak positions themselves and the shape of the peaks are modified indicating significant redox modulation due to the presence of both Au and cobalt oxide alongside copper oxide.

The varying amount of H_2O_2 detected using the RRDE, besides the changing potential dependent redox features, indicates that the mechanism of ORR currents on these electrodes is potential dependent.[44] The electron transfer kinetics were evaluated over a narrow potential window of 0.90 V–0.85 V. The kinetic currents were extracted from Koutecky–Levich plots (ESI note 2 and Fig. S6†). Tafel plots resulting from these kinetic currents have been reported in Fig. 2(e). The straight lines obtained for Tafel plots indicate that electron transfer mechanisms remain reasonably steady over this narrow potential range. The Tafel slopes for Cu[Co]O_x were obtained in the range of 59 to 66 mV per decade, indicating that mechanisms for e-transfer are very similar to that of pure CoO_x/Au electrodes. The pure-CuO_x/Au catalyst showed a higher onset potential (w.r.t. E^0 value of 1.23 V) and a higher Tafel slope (72 mV per decade). It is very likely that ORR active sites in the Cu[Co]O_x/Au electrodes are still located around Co ions in these oxides.

The electrochemically active surface area (ECSA) of various samples was measured using cyclic voltammetry at several potential scan rates (Fig. 2(f)) (more details can be found in ESI note 3 and Fig. S7 of the ESI†). The capacitance of the electrodes was calculated from the non-faradaic region of the CVs (between −0.46 V and −0.59 V for $Cu_{0.8}Co_{0.2}O_x$/Au, −0.49 V to −0.59 V for CuO_x/Au, and −0.60 V to −0.70 V for CoO_x/Au. The potentials used in the context of the ECSA are reported *vs.* Ag/AgCl). The ECSA was estimated by using a double-layer capacitance value of 40 μF cm^{-2} for flat electrodes. The CuO_x/Au electrode has the largest ECSA of 5.189 cm^2, followed by $Cu_{0.8}Co_{0.2}O_x$/Au (0.615 cm^2) and CoO_x/Au (0.398 cm^2).

Fig. 3(a) and (b) show potential dependent H_2O_2 yields and electron transfer numbers (n) between 0.9 and 0.4 V (calculations are reported in ESI note 1†). The n and H_2O_2 yields for pure-CuO_x/Au and CoO_x/Au catalysts show a high preference for the two-electron pathway, which increases with decreasing potential. However, the peroxide yield was in general low for Cu[Co]O_x/Au electrodes (especially those rich in the Cu content). Cu-rich $Cu_{0.8}Co_{0.2}O_x$/Au shows ~2.5% yield of peroxide, which was steady over a large potential window. Fuel cells typically operate at around ~0.7 V (two-electrode configuration), with only minor potential drops attributed to the hydrogen electrode. The ORR cathode typically operates between 0.7 and 0.6 V *versus* the RHE. This makes Cu-rich Cu[Co]O_x/Au electrodes reported here suitable for application in fuel cells. Fig. 3(c) lists the H_2O_2 selectivity and electron transferred numbers for various electrodes at 0.6 V. Meanwhile, H_2O_2 yields on pure-CoO_x/Au and CuO_x/Au electrodes are around 30% and 20%, respectively, and the yield on the Cu[Co]O_x/Au electrode remain below 10%. Specifically, the Cu-rich combination of $Cu_{0.6}Co_{0.4}O_x$/Au and $Cu_{0.8}Co_{0.2}O_x$/Au shows very low peroxide yields of ~4% and 2.5% respectively.

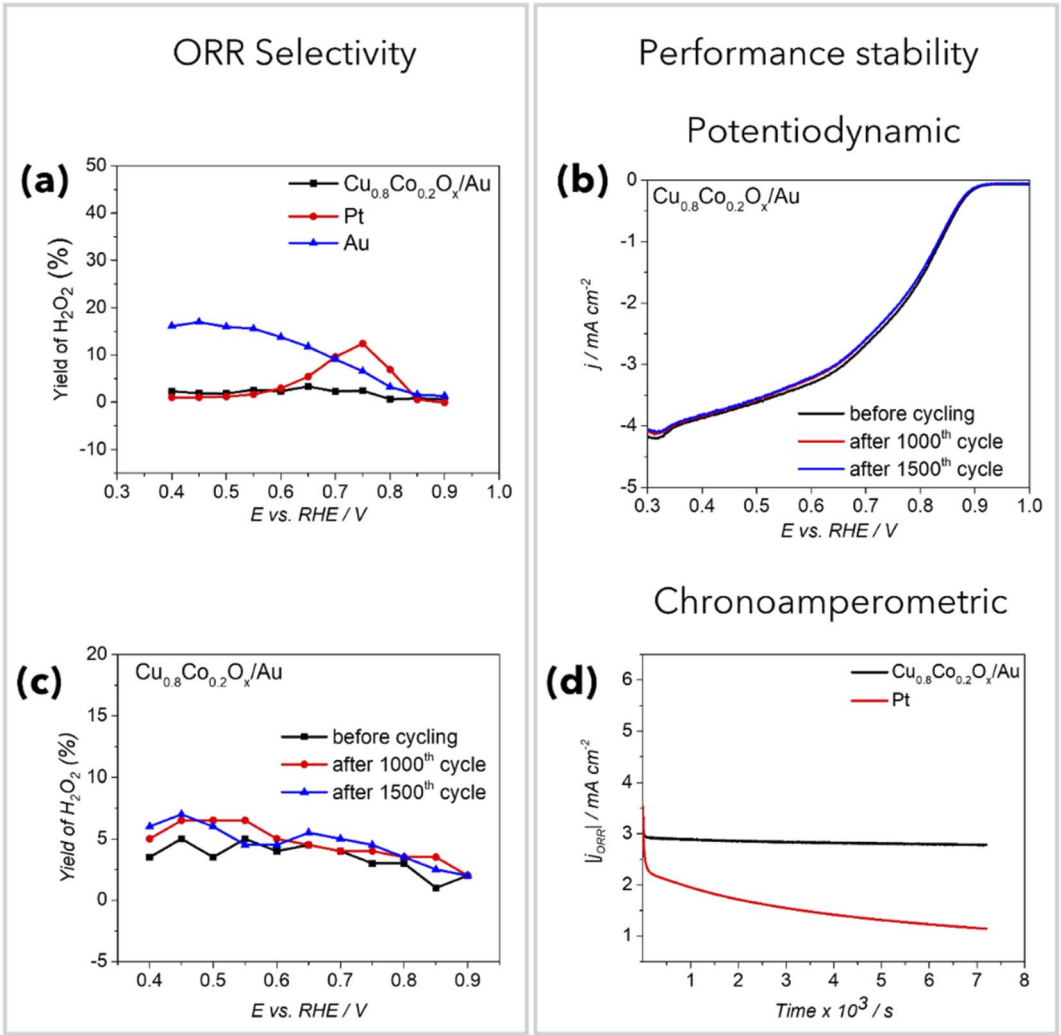

Fig. 4 (a) H_2O_2 yield as a function of potential is shown for Pt, Au, and doped-Cu[Co]O_x/Au electrodes. (b) RDE polarization curves of $Cu_{0.8}Co_{0.2}O_x$/Au in O_2-saturated 0.1 M NaOH (at 5 mV s^{-1} and 1600 rpm electrode rotation speed). The electrode was subject to potential cycling between 0.6 and 1.0 V at a scan rate of 50 mV s^{-1}. The polarization curves after the 1000th and 1500th potential cycles are compared to the initial polarization curve. (c) H_2O_2 yield (%) before and after the 1000th and 1500th cycles and (d) chronoamperometric performance of Cu[Co]O_x/Au ($Cu_{0.8}Co_{0.2}O_x$/Au) and Pt electrodes at 0.7 V in O_2-saturated 0.1 M NaOH. The electrode was rotated at 1600 RPM. $|j_{ORR}|$ has been plotted *vs.* time.

The representative Cu[Co]O_x/Au electrode, $Cu_{0.8}Co_{0.2}O_x$/Au, was compared to benchmarks such as polycrystalline Pt and Au electrodes (Fig. 4). The electrode ($Cu_{0.8}Co_{0.2}O_x$/Au) was found to outperform the benchmarks in terms of H_2O_2 selectivity (Fig. 4(a) and S8(a)†). Peroxide production on the Pt electrode increases starting at 0.85 V and reaches a peak of ~15% at 0.7 V, and then drops to less than 5% at ~0.6 V (Fig. 4(a)). Starting at 0.85 V, the peroxide production for the Au electrode gradually increases and reaches ~18% at ~0.4 V (Fig. 4(a)). In contrast, the $Cu_{0.8}Co_{0.2}O_x$/Au electrode performs well in the potential range of interest, *i.e.*, 0.9 to 0.4 V. The peroxide production remains below 2.5% over the indicated potential range, indicating that the $Cu_{0.8}Co_{0.2}O_x$/Au electrode exhibits consistent performance across the potential range of interest.

The performance stability of the electrodes was evaluated using potential cycling-based stress experiments over 0.6 to 1.0 V (practical for an ORR cathode operating in a fuel cell device) (Fig. 4(b)). Potential cycling of the Cu[Co]O_x/Au electrode up to 1500 times between these potentials (at 50 mV s^{-1}) did not result in any significant change in either activity or selectivity (Fig. 4(b) and (c)).

Furthermore, the chronoamperometric performance of the $Cu_{0.8}Co_{0.2}O_x$/Au electrode was compared with that of Pt by holding both electrodes at 0.7 V (Fig. 4(d)). The electrode performances degrade initially but stabilized later. The activity of the $Cu_{0.8}Co_{0.2}O_x$/Au electrode after 1000 s was ~85% of its initial value. The activity of the Pt electrode degraded to ~55% of its initial performance within the same time frame. Comparing the activities at 1000 and 7000 seconds, the Pt electrode showed a further activity loss of ~41%, which is significantly higher than the activity loss observed in the $Cu_{0.8}Co_{0.2}O_x$/Au electrode's performance (~3.6%) (Fig. S8(b)†).

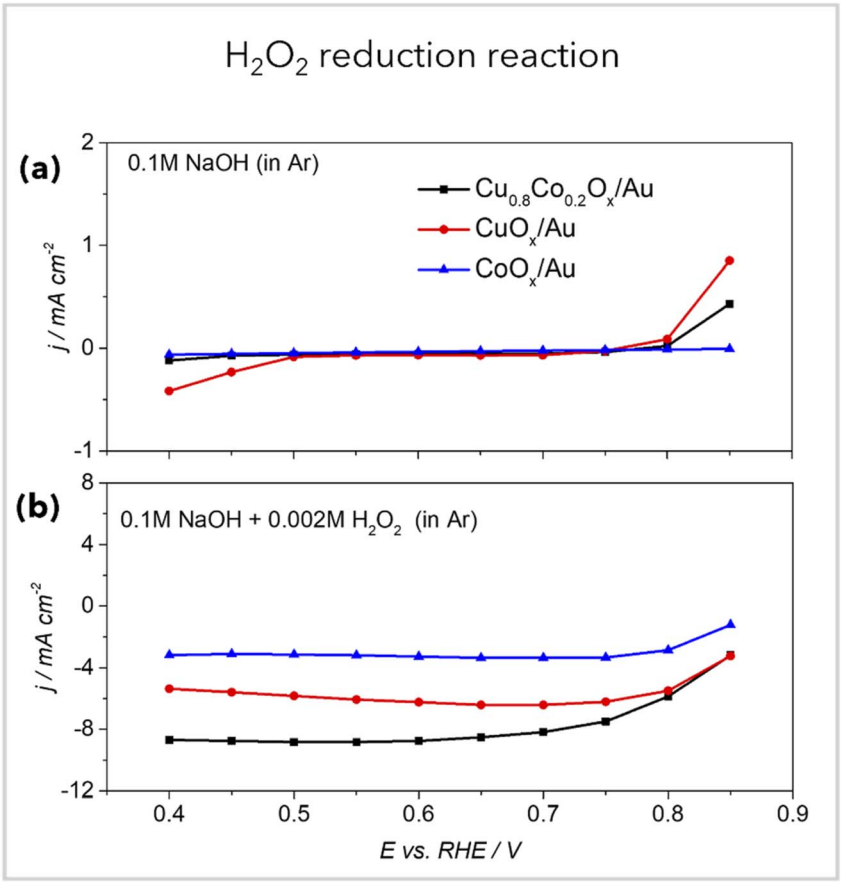

Fig. 5 Steady-state currents were obtained from chronoamperometry. $Cu_{0.8}Co_{0.2}O_x$/Au, CuO_x/Au, and CoO_x/Au electrodes in Ar saturated (a) 0.1 M NaOH and (b) 0.1 M NaOH + 2 mM H_2O_2. The electrode was rotated at 1600 rpm.

The absolute currents for Pt and $Cu_{0.8}Co_{0.2}O_x$/Au electrodes are shown in Fig. 4(d).

Cu-rich Cu[Co]O_x/Au electrodes were found to perform significantly better than either of pure CoO_x/Au and CuO_x/Au electrodes. This increase in performance may be attributed to the synergistic interactions between Co and Cu resulting in a mechanistic shift in the ORR. Specifically, one might attribute this improved performance to the ability of catalysts to handle peroxide.

Performance against H_2O_2 decomposition was tested using steady-state electrochemical experiments performed in solutions containing 2 mM H_2O_2 (Fig. 5). Both blank and H_2O_2 containing solutions were continuously purged with Ar (to remove any O_2 generated during these experiments), while the experiments were carried out between 0.85 and 0.4 V (potential step size of 0.5 V and holding time: 2 minutes at each potential). While the blank solution does not show any currents in the relevant potential range (Fig. 5(a)), significant faradaic currents attributable to H_2O_2 reduction were found in H_2O_2 containing solution (Fig. 5(b)). The $Cu_{0.8}Co_{0.2}O_x$/Au electrode significantly outperformed the pure CuO_x/Au and CoO_x/Au electrodes. This enhanced performance of doped-Cu[Co]O_x/Au against peroxide likely gets reflected in its ability to be highly selective for four-electron pathways during the ORR.

In situ Raman spectroscopy

In situ Raman Spectroscopy was used to study the catalyst structure over the potential range of interest.

Fig. 6 shows the *in situ* Raman spectra of the pure and doped-Cu[Co]O_x/Au catalysts. Table 2 shows the Raman bands of various relevant phases tabulated from the literature. Fig. 6(a) and (b) show the CuO_x/Au *in situ* Raman spectra in oxygen saturated 0.1 M NaOH. At potentials higher than 0.7 V, three Raman bands are observed at 301, 348, and 620 cm^{-1}, corresponding to the A_g and two B_g modes of the CuO (Cu^{2+}) phase respectively.[53–55] Below 0.7 V, which coincides with the reduction of $Cu^{2+} \rightarrow Cu^{1+}$ (Fig. 1(c)), these peaks vanished and four new peaks appeared at 150, 230, 525, and 631 cm^{-1}. These peaks can be assigned to the reduced phase Cu_2O (containing Cu^{1+} ions).[47,48] The disappearance of CuO peaks and the appearance of the Cu_2O peak at ~0.7 V indicate the phase change of the electrode material at this potential accompanying electrochemical reduction.

Fig. 6(c) shows the *in situ* Raman spectra of CoO_x/Au, with Raman bands at 198, 504, 636, and 696 cm^{-1}. The peaks at 198 cm^{-1} and 696 cm^{-1} correspond to the F_{2g} and A_{1g} modes of Co_3O_4 respectively.[50] The peaks at 504 cm^{-1} and 636 cm^{-1} correspond to CoO(OH), where 504 cm^{-1} refers to the E_g (Co–O stretching mode) of CoO(OH).[51,52,56] Over the entire ORR

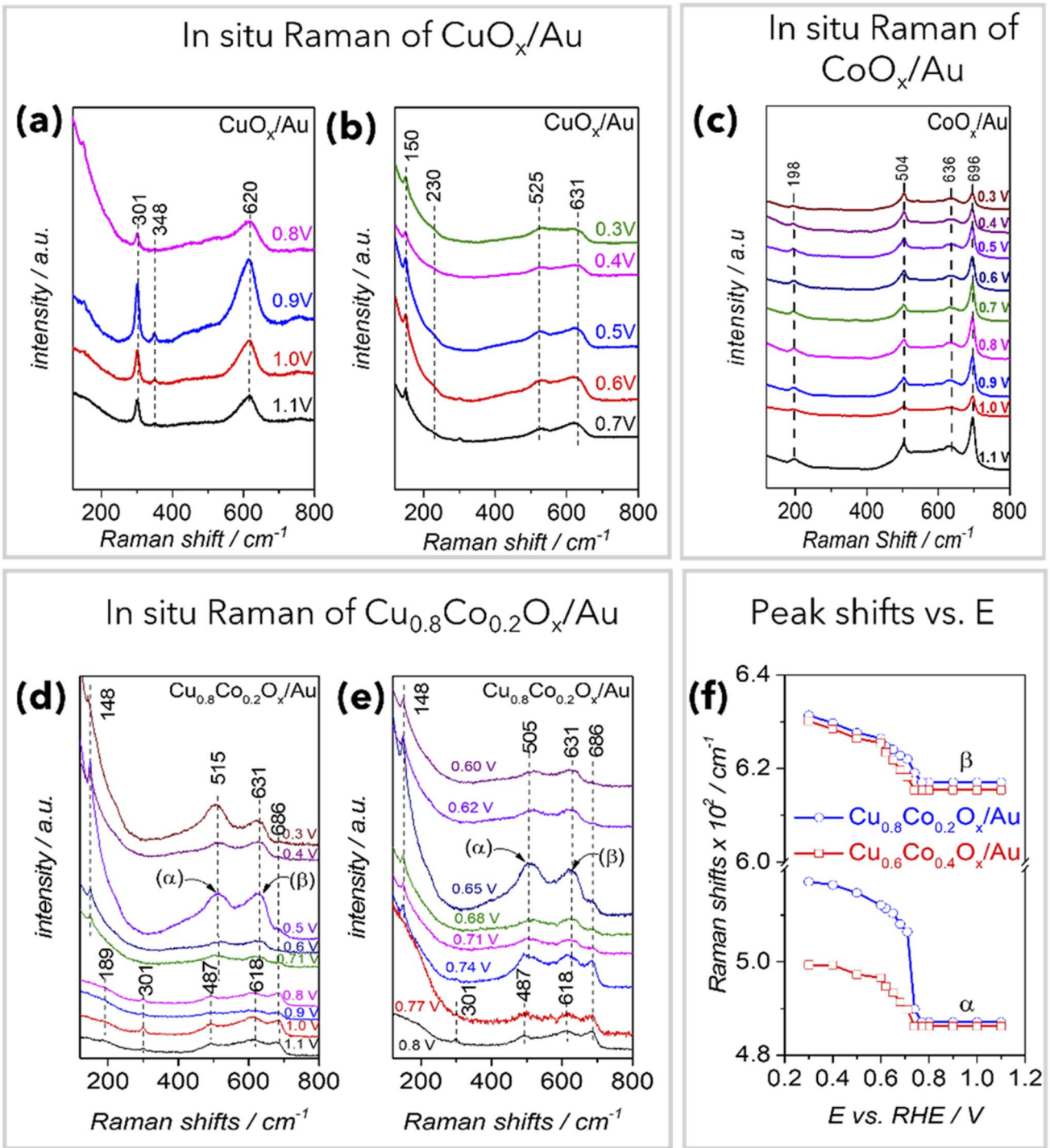

Fig. 6 *In situ* Raman spectroscopy of Cu[Co]O_x/Au electrodes in O_2 sat. 0.1 M NaOH. Potential is swept from 1.1 V to 0.3 V with a potential step size of 0.1 V. (a and b) CuO_x/Au, (c) CoO_x/Au, and (d) $Cu_{0.8}Co_{0.2}O_x$/Au, and (e) the Raman spectra shown here were collected on $Cu_{0.8}Co_{0.2}O_x$/Au between 0.8 V to 0.6 V at a small potential step size of 30 mV and (f) the potential-dependent position of α and β Raman bands in doped-Cu[Co]O_x/Au electrodes. Two compositions are shown.

potential range, the CoO_x/Au sample essentially remained multiphasic and did not change with applied potential.

Fig. 6(d) and (e) show the potential dependent *in situ* Raman spectra of the $Cu_{0.8}Co_{0.2}O_x$/Au catalyst. Five Raman bands are observed at 189, 301, 487, 618, and 686 cm^{-1} for $Cu_{0.8}Co_{0.2}O_x$/Au, from 1.1 V to 0.74 V. The peaks at 487, 618, and 686 cm^{-1} dominate the spectrum over a large potential range. The CuO component (301 cm^{-1}) which transforms into Cu_2O (148 cm^{-1}) at 0.74 V remains minor in comparison to the intensities observed amongst 487, 618, and 686 cm^{-1} bands. The 189 cm^{-1} and 686 cm^{-1} bands are associated with Co_3O_4 (Co^{2+}/Co^{3+}). The bands at 487 (α) and 618 cm^{-1} (β) can be associated with Co–O–

Table 2 Raman bands corresponding to pure phases of CuO_x and CoO_x

Phases	Raman bands (cm^{-1})	References
CuO	301, 348, 620	34, 45 and 46
Cu_2O	150, 230, 525, 631	47 and 48
$Cu(OH)_2$	487	34, 45 and 49
Co_3O_4	198, 696	50 and 51
CoO(OH)	504, 636	51 and 52

Cu metal–O stretching modes of a mixed Cu and Co phase.[50,54,57] The α and β bands were plotted as a function of potential (for doped electrodes with $y = 0.6$ and 0.8) (Fig. 6(f)). These bands remained invariant above 0.8 V but show a drastic blue shift around 0.7 V, which is associated with the reduction of Cu^{2+} to Cu^{1+}. Beyond this potential, a gradual blue shift was observed. At potentials around 0.6 V, the α and β bands form the majority of the spectrum. This indicates that doped-Cu[Co]O_x/Au is essentially composed of Co–O–Cu type linkages and the redox features of Cu ($Cu^{2+} \rightarrow Cu^{1+}$) result in the tuning of the M–O stretching frequency without undergoing a phase transition in contrast with what was observed in pure CuO_x/Au. It demonstrates that Cu centers remain close to Co through Co–O–Cu type connections and can significantly influence the electronic properties of the Co center. No specific evidence of CoO(OH) was observed in the doped-Cu[Co]O_x/Au spectrum.

XPS analysis

The surface chemical composition of $Cu_{0.8}Co_{0.2}O_x$/Au, CuO_x/Au, and CoO_x/Au was investigated using X-ray Photoelectron Spectroscopy (XPS). The samples include as-prepared samples and those treated at 0.9 V and 0.6 V under the ORR.

The Cu 2p spectra of the CuO_x/Au sample are shown in Fig. 7(a). Phase assignments remain complex in XPS spectra for Cu 2p levels, specifically in the context of mixed-phase samples.[58,59] The Cu 2p satellite features between 940 and 945 eV are indicative of Cu^{2+} species. These features are prominent in the as-prepared sample. Upon applying potential between 0.9 V and 0.6 V, the relative intensity of these satellite features progressively decreases affirming the Cu^{2+} to Cu^{1+} reduction. The broadening of the Cu 2p peak towards lower binding energy at 0.6 V is evident of the formation of Cu^{1+}

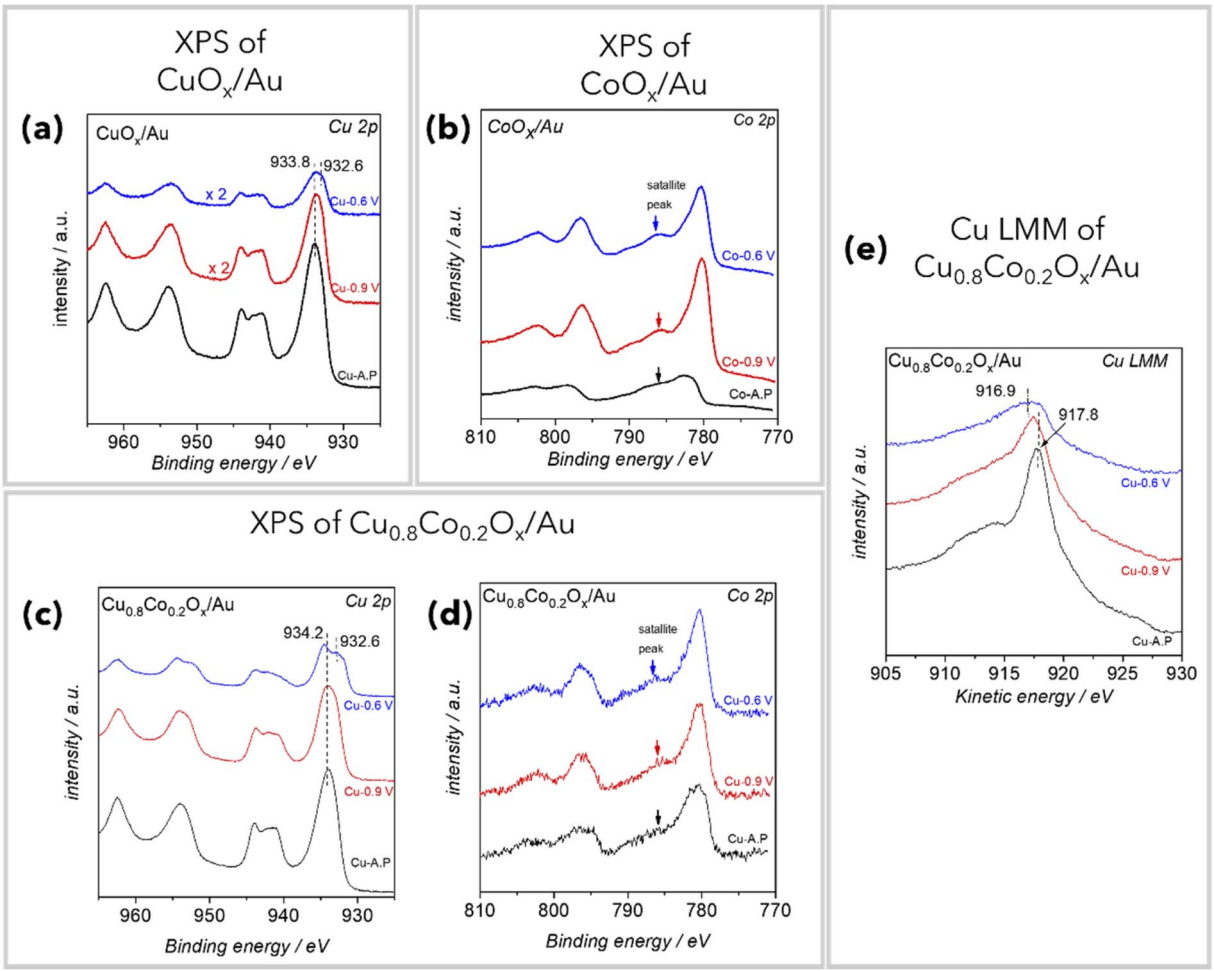

Fig. 7 XPS spectra collected under various conditions. (a) Cu 2p spectra of CuO_x/Au, (b) Co 2p spectra of CoO_x/Au, (c) Cu 2p spectra of $Cu_{0.8}Co_{0.2}O_x$/Au, (d) Co 2p spectra of $Cu_{0.8}Co_{0.2}O_x$/Au and (e) Cu LMM spectra of $Cu_{0.8}Co_{0.2}O_x$/Au.

species upon reduction.[58,59] This is in good agreement with the *in situ* Raman spectra (Fig. 6(a) and (b)), where the vibrational features associated with Cu–O vibration in CuO and Cu_2O were used to track the reduction of Cu ions in the sample.

Fig. 7(b) shows Co 2p XPS spectra for CoO_x/Au. Co 2p XPS spectra obtained from as-prepared samples and those treated at 0.6 and 0.9 V show insignificant differences, indicating that CoO_x/Au does not experience much change during the ORR, which is consistent with the results of our *in situ* Raman experiment. Significant overlapping of XPS peaks amongst CoO_x phases makes the assignment of distinct phases of CoO_x such as Co_3O_4, CoO(OH), and $Co(OH)_2$ difficult. The Co 2p peak for all these compounds occurs at ~280.4 ± 0.3 eV, all containing Co^{3+}.[51,60] The satellite feature at ~786 eV shows the presence of Co^{2+} species. Co_3O_4 identified in Raman experiments contains both Co^{2+} and Co^{3+} ions. The Raman spectra (Fig. 6(c)) showed peaks associated with Co_3O_4 and CoO(OH) phases, which is consistent with the presence of Co^{2+} and Co^{3+} species in XPS. As mentioned above, in XPS, the presence of CoO(OH) (which contains Co^{3+} ions) is difficult to distinguish from Co_3O_4 in a multiphasic sample. The as-prepared CoO_x/Au sample showed significant charging as evidenced by shifting of Co $2p_{3/2}$ XPS peaks to higher binding energies and broadening of the peaks. Likely, the thermally annealed as-prepared sample (rich in the Co_3O_4 phase) has poor conductivity compared to samples that have been electrochemically treated.

The Cu 2p spectra of the as-prepared $Cu_{0.8}Co_{0.2}O_x$/Au sample and sample treated at 0.9 V have a single peak ~934.2 eV and a satellite feature at 940–945 eV, which can be uniquely attributed to the Cu^{2+}-type of species (Fig. 7(c)). However, as we go from collected spectra of the as prepared sample to those treated at 0.9 V and 0.6 V, the intensity of the satellite peak progressively decreases (similar phenomenon observed in CuO_x/Au) and specifically upon holding the sample at 0.6 V (after ORR onset) one can see the emergence of a peak at 932.6 eV attributed to Cu^{1+} species (Fig. 7(c)). This indicates that there is reduction of Cu^{2+} to Cu^{1+} in the sample.[58,59] However, to further confirm the presence of Cu^{1+} species, we have also analysed the Auger parameters, *i.e.*, Cu LMM peaks (Fig. 7(e)). For the as-prepared sample, the peak at 917.8 eV and well-defined satellite peaks at (910 eV–915 eV) indicate the presence of Cu^{2+}.[58] However upon electrochemical treatment (0.9 V and 0.6 V under O_2), the peak at 917.8 eV shifts to lower KE values, indicating the reduction of Cu^{2+} species.[58] At 0.6 V, the satellite features disappeared and the peak shifted to 916.9 eV indicating the formation of Cu^{1+} species.[58] Peaks observed in the Raman spectra of the doped sample (Fig. 6(d) and (e)) do not indicate Cu–O vibrations associated with known CuO/Cu_2O phases in contrast to the pure CuO_x/Au sample. The change in the oxidation state of Cu can be tracked through stark tuning (shifting of band position with applied potential) of α and β bands (Fig. 6(f)), which shows a sharp blueshift at ~0.7 V, the potential associated with the electrochemical reduction of Cu^{2+} to Cu^{1+} (peak R^2) reported in the CV (Fig. 2(c) and Table 1). These observations from XPS and Raman are thus compatible.

Co 2p spectra for the doped sample (Fig. 7(d)) behave similarly to what was observed in the pure CoO_x/Au sample. The features primarily indicate the presence of Co^{2+} and Co^{3+} ions, which do not undergo any oxidation state change upon applying potentials relevant to the ORR.[51] Raman spectra (Fig. 6(c)–(e)) also indicate that the Co in the $Cu[Co]O_x$/Au material and CoO_x/Au does not undergo much phase change during the application of cathodic ORR potentials.

Mechanistic aspects

The primary structural difference between pure and Co-doped CuO_x ($Cu[Co]O_x$/Au) electrodes originates from the fact that doped electrodes are essentially an atomic level mixture of Cu and Co linked through Co–O–Cu type oxidic linkages. The similarity of Tafel slopes and the onset behaviour of the $Cu[Co]O_x$/Au electrode to pure Co oxides indicates that the Co center is very likely the active site for the ORR. The *in situ* Raman spectrum of the doped-$Cu[Co]O_x$/Au electrode shows that Co centers can be locked inside a $CuO_x(OH)_x$ matrix. In such a system, the reduction of Cu^{2+} to Cu^{1+} manifests through M–O frequency tuning with applied potential. A blueshift of α and β bands coincident with the electrochemical reduction peak (R^2 ~ 0.7 V) in CV is observed. We propose that it is this electronic tuning of the Co site through Cu, which results in the improved performance of the system. This material shows improved activity not only for the ORR but also for the reduction of H_2O_2 indicating that the surface comprising of Co–O–Cu can easily cleave O–O bonds, which gets reflected in its high selectivity for the 4e pathway in the context of the ORR.

Kou *et al.* have reported Co–Mo_2C heterostructures as OER catalysts.[61] During the early stages of the OER in Co–Mo_2C, the Co is transformed into Mo enriched defective γ-CoOOH, as evidenced by XPS, which aided OER kinetics. The performance enhancement has been explained through alteration of the Co electronic structure *via* Mo–O–Co bonding interaction that results in an optimum M–OH bond strength.[61] The synergistic effects of Cu–Co oxides have been explored by Niu *et al.* in the context of the oxygen evolution reaction (OER).[32] They have demonstrated high performance of $Co_{0.30}Cu_{0.7}O_x$ (30% Cu sites substituted by Co) for the OER. Using theoretical DFT calculations, they have shown that the incorporation of Co ions into the CuO lattice results in stronger binding of adsorbed O* at the Co site resulting in the reduction of free energy of the step and consequent alteration of the potential determining step. Similarly, the incorporation of Co into the Cu_2O lattice results in higher stabilization of Co–OOH* species compared to pure Cu_2O, resulting in lowering of the free energy of the potential determining step and thus leading to the reduction of overpotential.

Scheme 1 shows various steps in the electrochemical reduction of O_2 to water. We present our hypothesis based on structural evidence available to us from *in situ* Raman and *ex situ* XPS around Co sites in the CuO_x framework to explain our Co-doped CuO_x ($Cu[Co]O_x$/Au) catalysts' remarkable selectivity for the 4e pathway (Scheme 2). The Cu atom is coordinated by four O^{2-} ions in CuO and Cu_2O, forming a square planar and tetrahedral framework, respectively. The Cu–O bond lengths in CuO and Cu_2O are 1.96 and 1.86 Å respectively. When Co ions

$M + O_2 \rightarrow M\text{-}O_2^*$ ---(1)

$M\text{-}O_2^* + H_2O + e^- \rightarrow M\text{-}OOH^* + OH^-$ ---(2)

$M\text{-}OOH^* \rightarrow M\text{-}O^* + M\text{-}OH^*$ ---(3)

$M\text{-}O^* + H_2O + e^- \rightarrow M\text{-}OH^* + OH^-$ ---(4)

$[M\text{-}OH^* + e^- \rightarrow OH^-] \times 2$ ---(5)

* adsorbed species

Scheme 1 Various steps in the electrochemical reduction of O_2 to OH^-. M is the metal active site and (*) indicates adsorbed species.

get integrated into the CuO framework, they take the place of the Cu atom. In the CuO framework, the Co metal atom has now a square planar environment of bridging O^{2-} ions. In cobalt oxide phases, Co ions, regardless of the oxidation state, prefer to remain within an octahedral coordination environment with 6 oxygen ions surrounding the central Co ion, a coordination number (CN) of 6. The Co–O distance in Co_3O_4, $Co(OH)_2$, and CoOOH is 2.02 Å, 2.13 Å, and (1.88–2.25) Å, respectively, longer than that in Cu–O bonds. Since the distance between Co and Cu is 2.94 Å in an adjacent layer, the square planar geometry around Co will be twisted into a distorted square planner geometry to compensate for the under-coordination of Co and adjust the Co–O bond length. The relative under-coordination of the Co site (central Co ion surrounded by 4 oxygen ions, CN = 4, as opposed to CN = 6 within the undoped cobalt oxide phases) will result in the Co ion under stress making it an active site for the ORR. Models of the ORR reactivity proposed by Li *et al.* indicate that the binding energy of the M–O bond is directly linked to the barrier of O–O cleavage.[16] The stronger the M–O bond(s), the easier the O–O cleavage. We propose that the unsaturated/defective Co sites result in stronger binding of oxygen to the Co site making it easier to cleave the O–O bond. It is the ease of O–O bond cleavage which gets reflected in the higher selectivity for the 4e pathway. As per Scheme 1, molecular oxygen is likely to be reduced at the Co site to OOH* during the ORR (step 2). Due to under-coordination at the Co site, the O–O bond of OOH* species is likely to cleave more easily compared to that of pure CuO_x or CoO_x. This would explain the improved performance of $Cu[Co]O_x$/Au electrodes with regards to lower selectivity towards H_2O_2 formation during the ORR, and their improved performance against H_2O_2 reduction (Fig. 5(b)). Free energy calculations by Niu *et al.* on a Co incorporated CuO/Cu_2O system support our analysis.[32] Although these calculations are intended to explain OER activity, they are equally applicable to the context of the ORR since it's the reverse reaction. They show that substitution by Co results in higher stability of the OOH* species at the Co site in combination with significant stabilization of the Co–O* species (Scheme 1, step 3).[32] They have shown that the incorporation of Co into the Cu site makes O–O cleavage significantly downhill compared to the same step on pure CuO_x making O–O cleavage much easier on Co-incorporated CuO_x. This will explain lower selectivity for H_2O_2 formation during the ORR for Co-incorporated CuO_x. The fact that the Tafel slope is roughly 60 mV dec^{-1} supports the idea that the rate-limiting step is a chemical step preceded by a fast electrochemical pre-equilibrium step.[62,63] We hypothesize that the chemical step of O–O cleavage (Scheme 1, step 3) which follows OOH* formation is the rate-determining in this case

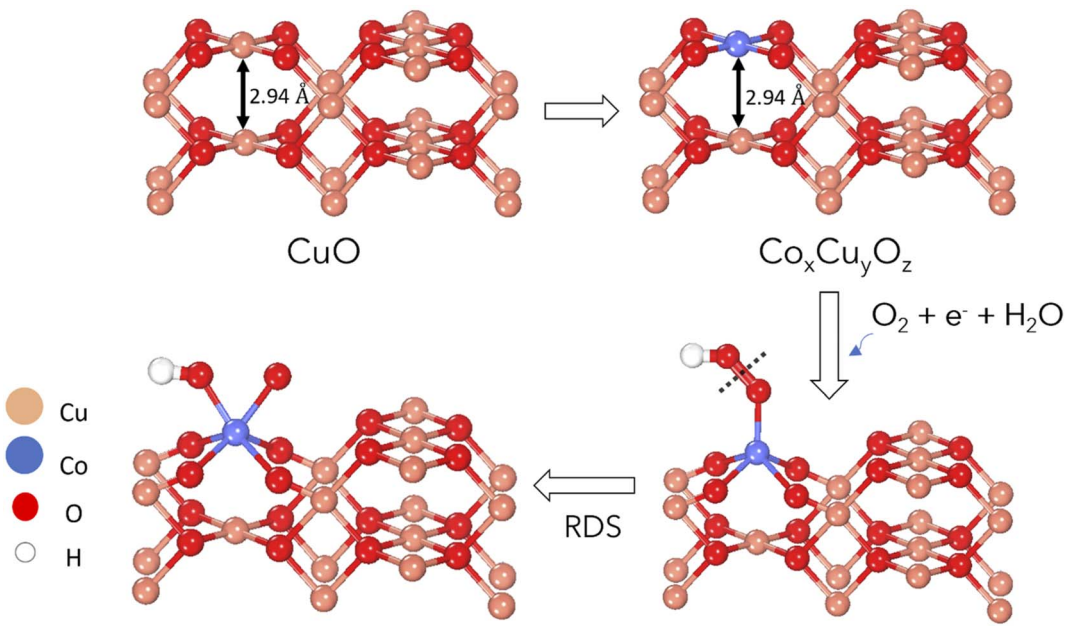

Scheme 2 Suggested mechanism of O–O bond cleavage at the Co site. During the ORR on $Cu[Co]O_x$ electrodes, the under-coordinated Co centers embedded within a CuO_x framework are likely to serve as the active sites for the cleavage of H_2O_2 to M–O and M–OH species.

(Scheme 2). The additional stabilization of Co–O* due to under-coordination at the Co site would result in lowering of the kinetic barrier for reaction 3 (O–O bond cleavage) as per the Sabatier principle.[64,65] In general, a defect at the Co site can result in both a stronger bond and a higher bond order for the Co–O bond. Defect sites do have the ability to multi-coordinate oxygen. This is also suggested by a paper from Li *et al.*, who have directly correlated the higher binding energy of the M–O bond with easier cleavage of the O–O bond.[16] Experimentally, Zhang *et al.* using EXAFS have shown that more defects can result in improved activity.[18]

Conclusion

We have reported a series of high-performing Co-doped CuO_x ($Cu[Co]O_x$/Au) ORR electrocatalysts supported on Au ($Cu[Co]O_x$/Au). We have demonstrated that the activity of the catalyst for the ORR increases with the Cu content. The $Cu_{0.8}Co_{0.2}O_x$/Au electrocatalyst in particular showed a remarkable ORR activity along with very low H_2O_2 selectivity. The optimal $Cu_{0.8}Co_{0.2}O_x$/Au catalyst produced relatively little peroxide (<2.5%) over a large potential range when compared to both pure CuO_x/Au (>18%) and pure CoO_x/Au (>30%) electrocatalysts. The H_2O_2 selectivity and ORR activity of $Cu_{0.8}Co_{0.2}O_x$/Au remain unaltered even after 1500 potential cycles. The catalyst was found to outperform even the Pt electrode, in terms of ORR activity, H_2O_2 selectivity, and performance stability. The doped-$Cu[Co]O_x$/Au electrodes outperformed the pure ones in the context of reduction of H_2O_2.

During the ORR, *in situ* Raman studies were used to track both pure and doped catalysts. We observed a phase change from CuO to Cu_2O during the ORR at ~0.7 V for the pure CuO_x/Au catalyst, whereas the pure CoO_x/Au catalyst largely remained multiphasic and did not change with applied potential over the ORR potential range. The presence of a Co–O–Cu framework in the Co-doped CuO_x ($Cu[Co]O_x$/Au) catalysts is revealed by the blueshifts of 487 (α) and 618 cm^{-1} (β) Raman bands along with the application of cathodic potentials. The bands associated with Cu–O vibrations in pure CuO/Cu_2O phases are not observed in the doped $Cu[Co]O_x$/Au electrode. Upon electrochemical reduction, the bands rather undergo a blueshift coincident with the electrochemical reduction of Cu^{2+} to Cu^{1+}. Both XPS and Auger spectra clearly indicate that Cu changes its oxidation state from Cu^{2+} to Cu^{1+}. This is unlike what is observed on pure CuO_x/Au electrodes, where peaks associated with CuO progressively disappear and those associated with Cu_2O appear upon electrochemical reduction (Cu^{2+} to Cu^{1+}). Ex-situ XPS spectra complement the Raman investigation.

We have hypothesized that the better activity and superior selectivity for the 4e pathway originate from electronic structure alteration of the active Co site incorporated in a CuO_x framework. The under-coordination environment around the Co site, CN 4 in the CuO_x framework as opposed to CN 6 in cobalt oxides, provides an optimal site for reducing O_2. It results in stronger binding of OOH* species at the Co site and makes O–O cleavage a more downhill reaction. We propose that it is this aspect of the catalyst that not only improves the kinetics of the rate-determining step but also enables a better selectivity for 4e products from the ORR and higher activity against H_2O_2 reduction.

We propose that the strategy of incorporating catalytic active sites into bonding frameworks that results in undercoordination/unsaturation at the active site can be a design principle for improving the activity and selectivity of catalysts.

Author contributions

SKB carried out experiments, data analysis and writing; CR was responsible for project conceptualisation, funding acquisition, experimental design, data analysis and writing.

Conflicts of interest

The authors declare no competing financial interest.

Acknowledgements

This study is supported in part by the Indian Institute of Science-Space Technology Cell (IISc-STC) (Grant No. 0430) and the Department of Science and Technology, India (SERB – CRG/2019/001586 and DST/TMD(EWO)/IC5-2018). SKB thanks the Indian Institute of Science for the PhD research fellowship.

References

1 P. G. Bruce, S. A. Freunberger, L. J. Hardwick and J.-M. Tarascon, Li–O_2 and Li–S Batteries with High Energy Storage, *Nat. Mater.*, 2012, **11**(1), 19–29, DOI: 10.1038/nmat3191.

2 Y. Nie, L. Li and Z. Wei, Recent Advancements in Pt and Pt-Free Catalysts for Oxygen Reduction Reaction, *Chem. Soc. Rev.*, 2015, **44**(8), 2168–2201, DOI: 10.1039/C4CS00484A.

3 Z. Peng, S. A. Freunberger, Y. Chen and P. G. Bruce, A Reversible and Higher-Rate Li-O2 Battery, *Science*, 2012, **337**(6094), 563–566, DOI: 10.1126/science.1223985.

4 L. Bu, N. Zhang, S. Guo, X. Zhang, J. Li, J. Yao, T. Wu, G. Lu, J.-Y. Ma, D. Su and X. Huang, Biaxially Strained PtPb/Pt Core/Shell Nanoplate Boosts Oxygen Reduction Catalysis, *Science*, 2016, **354**(6318), 1410–1414, DOI: 10.1126/science.aah6133.

5 X. Ge, A. Sumboja, D. Wuu, T. An, B. Li, F. W. T. Goh, T. S. A. Hor, Y. Zong and Z. Liu, Oxygen Reduction in Alkaline Media: From Mechanisms to Recent Advances of Catalysts, *ACS Catal.*, 2015, **5**(8), 4643–4667, DOI: 10.1021/acscatal.5b00524.

6 N. Ramaswamy, R. J. Allen and S. Mukerjee, Electrochemical Kinetics and X-Ray Absorption Spectroscopic Investigations of Oxygen Reduction on Chalcogen-Modified Ruthenium Catalysts in Alkaline Media, *J. Phys. Chem. C*, 2011, **115**(25), 12650–12664, DOI: 10.1021/jp201841j.

7 S. Tajik, H. Beitollahi, Z. Dourandish, P. Mohammadzadeh Jahani, I. Sheikhshoaie, M. B. Askari, P. Salarizadeh, F. G. Nejad, D. Kim, S. Y. Kim, R. S. Varma and M. Shokouhimehr, Applications of Non-precious Transition Metal Oxide Nanoparticles in Electrochemistry,

Electroanalysis, 2022, **34**(7), 1065–1091, DOI: **10.1002/elan.202100393**.

8 Q. Zhao, X. Tan, T. Ma, F. Cao, Z. Xia, H. Liu, H. Ning, Z. Li, H. Hu and M. Wu, Reinforced Atomically Dispersed Fe N C Catalysts Derived from Petroleum Asphalt for Oxygen Reduction Reaction, *J. Colloid Interface Sci.*, 2021, **587**, 810–819, DOI: **10.1016/j.jcis.2020.11.040**.

9 R. Jiang, L. Li, T. Sheng, G. Hu, Y. Chen and L. Wang, Edge-Site Engineering of Atomically Dispersed Fe–N $_4$ by Selective C–N Bond Cleavage for Enhanced Oxygen Reduction Reaction Activities, *J. Am. Chem. Soc.*, 2018, **140**(37), 11594–11598, DOI: **10.1021/jacs.8b07294**.

10 K. Liu, J. Fu, Y. Lin, T. Luo, G. Ni, H. Li, Z. Lin and M. Liu, Insights into the Activity of Single-Atom Fe-N-C Catalysts for Oxygen Reduction Reaction, *Nat. Commun.*, 2022, **13**(1), 2075, DOI: **10.1038/s41467-022-29797-1**.

11 I. Ledezma-Yanez, W. D. Z. Wallace, P. Sebastián-Pascual, V. Climent, J. M. Feliu and M. T. M. Koper, Interfacial Water Reorganization as a PH-Dependent Descriptor of the Hydrogen Evolution Rate on Platinum Electrodes, *Nat. Energy*, 2017, **2**(4), 17031, DOI: **10.1038/nenergy.2017.31**.

12 J. Rossmeisl, J. K. Nørskov, C. D. Taylor, M. J. Janik and M. Neurock, Calculated Phase Diagrams for the Electrochemical Oxidation and Reduction of Water over Pt(111), *J. Phys. Chem. B*, 2006, **110**(43), 21833–21839, DOI: **10.1021/jp0631735**.

13 J. K. Nørskov, T. Bligaard, A. Logadottir, S. Bahn, L. B. Hansen, M. Bollinger, H. Bengaard, B. Hammer, Z. Sljivancanin, M. Mavrikakis, Y. Xu, S. Dahl and C. J. H. Jacobsen, Universality in Heterogeneous Catalysis, *J. Catal.*, 2002, **209**(2), 275–278, DOI: **10.1006/jcat.2002.3615**.

14 J. Suntivich, H. A. Gasteiger, N. Yabuuchi, H. Nakanishi, J. B. Goodenough and Y. Shao-Horn, Design Principles for Oxygen-Reduction Activity on Perovskite Oxide Catalysts for Fuel Cells and Metal–Air Batteries, *Nat. Chem.*, 2011, **3**(7), 546–550, DOI: **10.1038/nchem.1069**.

15 J. Suntivich, K. J. May, H. A. Gasteiger, J. B. Goodenough and Y. Shao-Horn, A Perovskite Oxide Optimized for Oxygen Evolution Catalysis from Molecular Orbital Principles, *Science*, 2011, **334**(6061), 1383–1385, DOI: **10.1126/science.1212858**.

16 H. Li, S. Kelly, D. Guevarra, Z. Wang, Y. Wang, J. A. Haber, M. Anand, G. T. K. K. Gunasooriya, C. S. Abraham, S. Vijay, J. M. Gregoire and J. K. Nørskov, Analysis of the Limitations in the Oxygen Reduction Activity of Transition Metal Oxide Surfaces, *Nat. Catal.*, 2021, **4**(6), 463–468, DOI: **10.1038/s41929-021-00618-w**.

17 Y. Cao, M. J. Gadre, A. T. Ngo, S. B. Adler and D. D. Morgan, Factors Controlling Surface Oxygen Exchange in Oxides, *Nat. Commun.*, 2019, **10**(1), 1346, DOI: **10.1038/s41467-019-08674-4**.

18 R. Zhang, Y.-C. Zhang, L. Pan, G.-Q. Shen, N. Mahmood, Y.-H. Ma, Y. Shi, W. Jia, L. Wang, X. Zhang, W. Xu and J.-J. Zou, Engineering Cobalt Defects in Cobalt Oxide for Highly Efficient Electrocatalytic Oxygen Evolution, *ACS Catal.*, 2018, **8**(5), 3803–3811, DOI: **10.1021/acscatal.8b01046**.

19 Z.-L. Wang, D. Xu, J.-J. Xu and X.-B. Zhang, Oxygen Electrocatalysts in Metal–Air Batteries: From Aqueous to Nonaqueous Electrolytes, *Chem. Soc. Rev.*, 2014, **43**(22), 7746–7786, DOI: **10.1039/C3CS60248F**.

20 J.-L. Shui, J. S. Okasinski, P. Kenesei, H. A. Dobbs, D. Zhao, J. D. Almer and D.-J. Liu, Reversibility of Anodic Lithium in Rechargeable Lithium–Oxygen Batteries, *Nat. Commun.*, 2013, **4**(1), 2255, DOI: **10.1038/ncomms3255**.

21 F. Bidrawn, S. Lee, J. M. Vohs and R. J. Gorte, The Effect of Ca, Sr, and Ba Doping on the Ionic Conductivity and Cathode Performance of $LaFeO_3$, *J. Electrochem. Soc.*, 2008, **155**(7), B660–B665, DOI: **10.1149/1.2907431**.

22 R. Martínez-Coronado, A. Aguadero, C. de la Calle, M. T. Fernández and J. A. Alonso, Evaluation of the R2RuMnO7 Pyrochlores as Cathodes in Solid-Oxide Fuel Cells, *J. Power Sources*, 2011, **196**(9), 4181–4186, DOI: **10.1016/j.jpowsour.2010.08.091**.

23 Y. Liang, Y. Li, H. Wang, J. Zhou, J. Wang, T. Regier and H. Dai, Co3O4 Nanocrystals on Graphene as a Synergistic Catalyst for Oxygen Reduction Reaction, *Nat. Mater.*, 2011, **10**(10), 780–786, DOI: **10.1038/nmat3087**.

24 D. U. Lee, P. Xu, Z. P. Cano, A. G. Kashkooli, M. G. Park and Z. Chen, Recent Progress and Perspectives on Bi-Functional Oxygen Electrocatalysts for Advanced Rechargeable Metal–Air Batteries, *J. Mater. Chem. A*, 2016, **4**(19), 7107–7134, DOI: **10.1039/C6TA00173D**.

25 X. Deng and H. Tüysüz, Cobalt-Oxide-Based Materials as Water Oxidation Catalyst: Recent Progress and Challenges, *ACS Catal.*, 2014, **4**(10), 3701–3714, DOI: **10.1021/cs500713d**.

26 J. E. Huheey, E. A. Keiter, R. L. Keiter and O. K. Medhi, *Inorganic Chemistry: Principles of Structure and Reactivity*, Pearson Education India, 2006.

27 K. L. Stewart and A. A. Gewirth, Mechanism of Electrochemical Reduction of Hydrogen Peroxide on Copper in Acidic Sulfate Solutions, *Langmuir*, 2007, **23**(19), 9911–9918, DOI: **10.1021/la7013557**.

28 X.-Y. Yan, X.-L. Tong, Y.-F. Zhang, X.-D. Han, Y.-Y. Wang, G.-Q. Jin, Y. Qin and X.-Y. Guo, Cuprous Oxide Nanoparticles Dispersed on Reduced Graphene Oxide as an Efficient Electrocatalyst for Oxygen Reduction Reaction, *Chem. Commun.*, 2012, **48**(13), 1892, DOI: **10.1039/c2cc17537a**.

29 I. Vincent, Electrochemical Characterization and Oxygen Reduction Kinetics of Cu-Incorporated Cobalt Oxide Catalyst, *Int. J. Electrochem. Sci.*, 2016, 8002–8015, DOI: **10.20964/2016.09.12**.

30 T. Grewe, X. Deng, C. Weidenthaler, F. Schüth and H. Tüysüz, Design of Ordered Mesoporous Composite Materials and Their Electrocatalytic Activities for Water Oxidation, *Chem. Mater.*, 2013, **25**(24), 4926–4935, DOI: **10.1021/cm403153u**.

31 M. D. Koninck, P. Manseau and B. Marsan, Preparation and Characterization of Nb-Doped TiO2 Nanoparticles Used as a Conductive Support for Bifunctional CuCo2O4 Electrocatalyst, *J. Electroanal. Chem.*, 2007, **611**(1–2), 67–79, DOI: **10.1016/j.jelechem.2007.08.004**.

32 W. Niu, J. Shi, L. Ju, Z. Li, N. Orlovskaya, Y. Liu and Y. Yang, Understanding Synergism of Cobalt Metal and Copper Oxide toward Highly Efficient Electrocatalytic Oxygen Evolution, *ACS Catal.*, 2018, **8**(12), 12030–12040, DOI: **10.1021/acscatal.8b03702**.

33 Z. Chen, C. X. Kronawitter, X. Yang, Y. Yeh, N. Yao and B. E. Koel, The Promoting Effect of Tetravalent Cerium on the Oxygen Evolution Activity of Copper Oxide Catalysts, *Phys. Chem. Chem. Phys.*, 2017, **19**(47), 31545–31552, DOI: **10.1039/C7CP05248K**.

34 Y. Deng, A. D. Handoko, Y. Du, S. Xi and B. S. Yeo, In Situ Raman Spectroscopy of Copper and Copper Oxide Surfaces during Electrochemical Oxygen Evolution Reaction: Identification of CuIII Oxides as Catalytically Active Species, *ACS Catal.*, 2016, **6**(4), 2473–2481, DOI: **10.1021/acscatal.6b00205**.

35 C. M. Sánchez-Sánchez and A. J. Bard, Hydrogen Peroxide Production in the Oxygen Reduction Reaction at Different Electrocatalysts as Quantified by Scanning Electrochemical Microscopy, *Anal. Chem.*, 2009, **81**(19), 8094–8100, DOI: **10.1021/ac901291v**.

36 M. K. Debe, Electrocatalyst Approaches and Challenges for Automotive Fuel Cells, *Nature*, 2012, **486**(7401), 43–51, DOI: **10.1038/nature11115**.

37 R. Borup, J. Meyers, B. Pivovar, Y. S. Kim, R. Mukundan, N. Garland, D. Myers, M. Wilson, F. Garzon, D. Wood, P. Zelenay, K. More, K. Stroh, T. Zawodzinski, J. Boncella, J. E. McGrath, M. Inaba, K. Miyatake, M. Hori, K. Ota, Z. Ogumi, S. Miyata, A. Nishikata, Z. Siroma, Y. Uchimoto, K. Yasuda, K. Kimijima and N. Iwashita, Scientific Aspects of Polymer Electrolyte Fuel Cell Durability and Degradation, *Chem. Rev.*, 2007, **107**(10), 3904–3951, DOI: **10.1021/cr050182l**.

38 Y.-C. Liu, C.-C. Wang and C.-E. Tsai, Effects of Electrolytes Used in Roughening Gold Substrates by Oxidation–Reduction Cycles on Surface-Enhanced Raman Scattering, *Electrochem. Commun.*, 2005, **7**(12), 1345–1350, DOI: **10.1016/j.elecom.2005.09.030**.

39 J.-C. Dong, X.-G. Zhang, V. Briega-Martos, X. Jin, J. Yang, S. Chen, Z.-L. Yang, D.-Y. Wu, J. M. Feliu, C. T. Williams, Z.-Q. Tian and J.-F. Li, In Situ Raman Spectroscopic Evidence for Oxygen Reduction Reaction Intermediates at Platinum Single-Crystal Surfaces, *Nat. Energy*, 2019, **4**(1), 60–67, DOI: **10.1038/s41560-018-0292-z**.

40 A. Das, B. Mohapatra, V. Kamboj and C. Ranjan, Promotion of Electrochemical Water Oxidation Activity of Au Supported Cobalt Oxide upon Addition of Cr: Insights Using in Situ Raman Spectroscopy, *ChemCatChem*, 2021, **13**(8), 2053–2063, DOI: **10.1002/cctc.202001889**.

41 F. Caballero-Briones, J. M. Artés, I. Díez-Pérez, P. Gorostiza and F. Sanz, Direct Observation of the Valence Band Edge by in Situ ECSTM-ECTS in p-Type Cu2O Layers Prepared by Copper Anodization, *J. Phys. Chem. C*, 2009, **113**(3), 1028–1036, DOI: **10.1021/jp805915a**.

42 S. M. Abd el Haleem and B. G. Ateya, Cyclic Voltammetry of Copper in Sodium Hydroxide Solutions, *J. Electroanal. Chem. Interfacial Electrochem.*, 1981, **117**(2), 309–319, DOI: **10.1016/S0022-0728(81)80091-5**.

43 S. D. Giri and A. Sarkar, Electrochemical Study of Bulk and Monolayer Copper in Alkaline Solution, *J. Electrochem. Soc.*, 2016, **163**(3), H252–H259, DOI: **10.1149/2.0071605jes**.

44 R. Zhou, Y. Zheng, M. Jaroniec and S.-Z. Qiao, Determination of the Electron Transfer Number for the Oxygen Reduction Reaction: From Theory to Experiment, *ACS Catal.*, 2016, **6**(7), 4720–4728, DOI: **10.1021/acscatal.6b01581**.

45 J. C. Hamilton, J. C. Farmer and R. J. Anderson, In Situ Raman Spectroscopy of Anodic Films Formed on Copper and Silver in Sodium Hydroxide Solution, *J. Electrochem. Soc.*, 1986, **133**(4), 739, DOI: **10.1149/1.2108666**.

46 X. K. Chen, J. C. Irwin and J. P. Franck, Evidence for a Strong Spin-Phonon Interaction in Cupric Oxide, *Phys. Rev. B*, 1995, **52**(18), R13130–R13133, DOI: **10.1103/PhysRevB.52.R13130**.

47 A. Singhal, M. R. Pai, R. Rao, K. Pillai, I. Lieberwirth and A. K. Tyagi, Copper(I) Oxide Nanocrystals – One Step Synthesis, Characterization, Formation Mechanism, and Photocatalytic Properties, *Eur. J. Inorg. Chem.*, 2013, **2013**(14), 2640–2651, DOI: **10.1002/ejic.201201382**.

48 G. Niaura, Surface-Enhanced Raman Spectroscopic Observation of Two Kinds of Adsorbed OH^- Ions at Copper Electrode, *Electrochim. Acta*, 2000, **45**(21), 3507–3519, DOI: **10.1016/S0013-4686(00)00434-5**.

49 D. Reyter, M. Odziemkowski, D. Bélanger and L. Roué, Electrochemically Activated Copper Electrodes: Surface Characterization, Electrochemical Behavior, and Properties for the Electroreduction of Nitrate, *J. Electrochem. Soc.*, 2007, **154**(8), K36, DOI: **10.1149/1.2746805**.

50 V. G. Hadjiev, M. N. Iliev and I. V. Vergilov, The Raman Spectra of Co3O4, *J. Phys. C: Solid State Phys.*, 1988, **21**(7), L199, DOI: **10.1088/0022-3719/21/7/007**.

51 J. Yang, H. Liu, W. N. Martens and R. L. Frost, Synthesis and Characterization of Cobalt Hydroxide, Cobalt Oxyhydroxide, and Cobalt Oxide Nanodiscs, *J. Phys. Chem. C*, 2010, **114**(1), 111–119, DOI: **10.1021/jp908548f**.

52 T. Pauporté, L. Mendoza, M. Cassir, M. C. Bernard and J. Chivot, Direct Low-Temperature Deposition of Crystallized CoOOH Films by Potentiostatic Electrolysis, *J. Electrochem. Soc.*, 2004, **152**(2), C49, DOI: **10.1149/1.1842044**.

53 J. C. Irwin, J. Chrzanowski, T. Wei, D. J. Lockwood and A. Wold, Raman Scattering from Single Crystals of Cupric Oxide, *Phys. C*, 1990, **166**(5), 456–464, DOI: **10.1016/0921-4534(90)90044-F**.

54 L. Debbichi, M. C. Marco de Lucas, J. F. Pierson and P. Krüger, Vibrational Properties of CuO and Cu4O3 from First-Principles Calculations, and Raman and Infrared Spectroscopy, *J. Phys. Chem. C*, 2012, **116**(18), 10232–10237, DOI: **10.1021/jp303096m**.

55 A. G. M. da Silva, T. S. Rodrigues, A. L. A. Parussulo, E. G. Candido, R. S. Geonmonond, H. F. Brito, H. E. Toma and P. H. C. Camargo, Controlled Synthesis of Nanomaterials at the Undergraduate Laboratory: $Cu(OH)_2$ and CuO Nanowires, *J. Chem. Educ.*, 2017, **94**(6), 743–750, DOI: **10.1021/acs.jchemed.6b00185**.

56 A. Moysiadou, S. Lee, C.-S. Hsu, H. M. Chen and X. Hu, Mechanism of Oxygen Evolution Catalyzed by Cobalt Oxyhydroxide: Cobalt Superoxide Species as a Key Intermediate and Dioxygen Release as a Rate-Determining Step, *J. Am. Chem. Soc.*, 2020, **142**(27), 11901–11914, DOI: 10.1021/jacs.0c04867.

57 X. Chen, D. A. Henckel, U. O. Nwabara, Y. Li, A. I. Frenkel, T. T. Fister, P. J. A. Kenis and A. A. Gewirth, Controlling Speciation during CO_2 Reduction on Cu-Alloy Electrodes, *ACS Catal.*, 2020, **10**(1), 672–682, DOI: 10.1021/acscatal.9b04368.

58 M. C. Biesinger, Advanced Analysis of Copper X-Ray Photoelectron Spectra: Advanced Analysis of Copper X-Ray Photoelectron Spectra, *Surf. Interface Anal.*, 2017, **49**(13), 1325–1334, DOI: 10.1002/sia.6239.

59 M. C. Biesinger, L. W. M. Lau, A. R. Gerson and R. St. C. Smart, Resolving Surface Chemical States in XPS Analysis of First Row Transition Metals, Oxides and Hydroxides: Sc, Ti, V, Cu and Zn, *Appl. Surf. Sci.*, 2010, **257**(3), 887–898, DOI: 10.1016/j.apsusc.2010.07.086.

60 M. C. Biesinger, B. P. Payne, A. P. Grosvenor, L. W. M. Lau, A. R. Gerson and R. St. C. Smart, Resolving Surface Chemical States in XPS Analysis of First Row Transition Metals, Oxides and Hydroxides: Cr, Mn, Fe, Co and Ni, *Appl. Surf. Sci.*, 2011, **257**(7), 2717–2730, DOI: 10.1016/j.apsusc.2010.10.051.

61 Z. Kou, Y. Yu, X. Liu, X. Gao, L. Zheng, H. Zou, Y. Pang, Z. Wang, Z. Pan, J. He, S. J. Pennycook and J. Wang, Potential-Dependent Phase Transition and Mo-Enriched Surface Reconstruction of γ-CoOOH in a Heterostructured Co-Mo_2C Precatalyst Enable Water Oxidation, *ACS Catal.*, 2020, **10**(7), 4411–4419, DOI: 10.1021/acscatal.0c00340.

62 A. J. Bard and L. R. Faulkner, *Electrochemical Methods: Fundamentals and Applications*, Wiley, New York, 2nd edn, 2001.

63 E. Gileadi, *Electrode Kinetics for Chemists, Chemical Engineers, and Materials Scientists*, VCH, 1993.

64 J. K. Nørskov, T. Bligaard, B. Hvolbæk, F. Abild-Pedersen, I. Chorkendorff and C. H. Christensen, The Nature of the Active Site in Heterogeneous Metal Catalysis, *Chem. Soc. Rev.*, 2008, **37**(10), 2163–2171, DOI: 10.1039/B800260F.

65 T. Bligaard, J. K. Nørskov, S. Dahl, J. Matthiesen, C. H. Christensen and J. Sehested, The Brønsted–Evans–Polanyi Relation and the Volcano Curve in Heterogeneous Catalysis, *J. Catal.*, 2004, **224**(1), 206–217, DOI: 10.1016/j.jcat.2004.02.034.